The effect of post-sintering treatments on the fatigue and biological behavior of Ti-6Al-4V ELI parts made by Selective Laser Melting

M. Benedetti[1*], E. Torresani[1], M. Leoni[2], V. Fontanari[1], M. Bandini[3], C. Pederzolli[4], C. Potrich[4,5]

[1]Department of Industrial Engineering, University of Trento, Trento, Italy

[2]Department of Civil, Environmental and Mechanical Engineering, University of Trento, Trento, Italy

[3]Peen Service Ltd, Bologna, Italy

[4]Laboratory of Biomolecular Sequence and Structure Analysis for Health, Fondazione Bruno Kessler, Trento, Italy

[5]Institute of Biophysics, CNR, Trento, Italy

*Contacting Author:

Matteo Benedetti

Tel. +390461282457

Fax +390461281977

E-mail: matteo.benedetti@unitn.it

Abstract

Fatigue resistance and biocompatibility are key parameters for the successful implantation of hard-tissue prostheses, which nowadays are more and more frequently manufactured by selective laser melting (SLM). For this purpose, the present paper is aimed at investigating the effect of post-sintering treatments on the fatigue behavior and biological properties of Ti samples produced by SLM. After the building process, all samples are heat treated to achieve a complete stress relief. The remaining ones are tribofinished with the aim of reducing the surface roughness of the as-sintered condition. Part of the tribofinished samples are then subjected to one of the following post-sintering treatments: (i) shot peening, (ii) hot isostatic pressing (HIP), and (iii) electropolishing. It is found that shot peening and HIP are the most effective treatments to improve

the high and the very-high cycle fatigue resistance, respectively. At the same time, they preserve the good biocompatibility ensured by the biomedical Titanium Grade 23.

Keywords

Selective laser melting; Ti-6Al-4V ELI; fatigue; shot peening; hot isostatic pressing; biocompability

Nomenclature

AM	additive manufacturing
c_1, c_2, m	parameters of Eq. (1) used to fit fatigue data
ELI	extra low interstitials
HC	high cycle
HIP	hot isostatic pressing
R	load ratio
S^2	estimated regression variance (Eq. (2))
SLM	selective laser melting
SLS	selective laser sintering
VHC	very high cycle
σ_a	axial stress amplitude

1. Introduction

1.1 Background

The substitution of human body parts with biomedical metallic devices, like joint prostheses or dental implants, is a tremendous medical and technological challenge, even in view of the longer human life expectancy and the implantation in younger patients. Accordingly, prostheses must contemporarily guarantee mechanical strength, biocompatibility and osseointegration over a time scale exceeding at least two decades. Standard metallic orthopedic materials include stainless steels, cobalt-base alloys, and titanium-base alloys, with an increasing number of devices being made of titanium alloys (Park and Lakes, 1992). However, titanium implants with complicated shapes can be hard machined from cast or wrought bars using traditional

subtractive technologies, like milling and turning, due to the high energy density necessary to remove material. Conversely, additive manufacturing (AM) methods appear to be a very promising and attractive technology. In addition, AM is the only viable solution when it is necessary to tailor a specific product to the patient anatomic conditions and produce it on demand, or to produce porous or cellular structures with adequate mechanical strength and desired elastic properties in order to fit the implant stiffness to that of the surrounding tissues (L. E. Murr et al., 2010) (Campoli et al., 2013; SU et al., 2012) (Hedayati et al., 2016) (Barriuso et al., 2014; Lipinski et al., 2013).

AM constitutes a heterogeneous group of different processes, basically distinguished on the heat source used to consolidate the material (Frazier, 2014; Froes and Dutta, 2014), i.e. electron beam (Collins et al., 2014; Facchini et al., 2009; Frazier, 2014; Froes and Dutta, 2014; Murr et al., 2012; Parthasarathy et al., 2010) laser, or arc (Frazier, 2014; Froes and Dutta, 2014; Leuders et al., 2013; Yu et al., 2012), and on how the raw material is supplied either in powder or wire. Laser based AM techniques such as selective laser sintering/melting (SLS/SLM) are gaining increasing interest in the biomedical context (Levy, 2010). The border that distinguishes SLS and SLM is rather vague. These two techniques differ in the laser's energy and consequently in the binding mechanisms that cause the powder consolidation (Kruth et al., 2005). Through SLS, the bind is obtained owing to liquid phase sintering or a partial fusion of powder particles. In this case, a post treatment is usually necessary to achieve higher mechanical properties and increase the density of the components. Conversely, through SLM, the powder particles are fully molten. In SLS/SLM the component is built layer-by-layer: the 3D geometry is decomposed into slices and each of them is manufactured through progressive deposition of a powder bed and its selective consolidation using a laser as heat source.

Although AM is capable to produce complex biomedical parts with improved biocompatibility, the mechanical properties of these products are still a great concern. The real SLS/SLM components generally show characteristic cast structure, with high superficial roughness, porosity, heterogeneous microstructure, and residual stresses, which negatively affect the mechanical properties. Therefore in order to reduce this defectiveness, the process must be carefully tuned in terms of scanning velocity, laser power and spot size (Kasperovich and Hausmann, 2015).

The high thermal gradients arising during the fast solidification process and the resulting internal stresses (Fergani et al., 2017) cannot be avoided and it is necessary to evaluate and/or mitigate their effects on the

mechanical properties. Accordingly, a post processing heat treatment is necessary to relieve these stresses before proceeding with any other secondary operation. Moreover, the high cooling rate also affects the microstructure, which is composed of an acicular/lamellar α' hcp phase (martensitic), a metastable phase of the α+β alloy as Ti-6Al-4V. This finer microstructure is less ductile than the globular one formed with the conventional processes. A microstructure similar to that typical of Ti-6Al-4V can be restored through a heat treatment above β transus (980°C) (Sercombe et al., 2008; Vilaro et al., 2011). The lamellar structure provides higher ductility (Murr et al., 2009; Pederson, 2002; Spierings et al., 2013) and fracture toughness (Benedetti et al., 2006), though tensile and fatigue strength are slightly lower than those of conventional bi-modal microstructures (Benedetti and Fontanari, 2004; Facchini et al., 2010). Another characteristic that must be taken into account when evaluating production of AM components is the anisotropy in microstructure and properties of SLS/SLM products (Baufeld et al., 2011; Brandl et al., 2011; Qiu et al., 2013). The directional nature of the process consequently affects the directionality of the characteristics of AM components. Therefore the structural and performance homogeneity of AM products can be influenced by the direction and inclination of their layers.

The SLS/SLM components are affected by the presence of internal porosity, which impacts very detrimentally on the mechanical properties. This defectiveness can have different origin as initial powder contaminations, entrapped gas bubble and lack of fusion (Brandl et al., 2012; Gorny et al., 2011; Lawrence E. Murr et al., 2010; Vilaro et al., 2012). Pores act as strong stress raisers promoting fatigue damage. Their minimization can be even more important than the microstructure optimization when the SLM products undergo cyclic loading and hence are prone to fatigue failure (Leuders et al., 2013). With the current technology, pore-like defects cannot be entirely avoided. However, it is largely demonstrated that the hot isostatic pressing (so called HIP process), a technology traditionally used in the powder metallurgy to achieve the full density, can substantially reduce or even close the pores present in SLS/SLM components (Agarwala et al., 1995; Santos et al., 2004; Yu et al., 2012). During this treatment, high temperature and high pressure are concomitantly applied to induce plastic flow and consequent full densification of the part. Usually, HIP treatments are performed above the β-transus temperature, so as to restore the lamellar α+β microstructure.

The surface condition is of paramount importance in prosthetic implants, as, on one hand, it controls the biological anchorage for the tissue in-growth and on the other one greatly affects the fatigue response. Kasperovich and Hausmann (Kasperovich and Hausmann, 2015) studied the effect of surface machining of SLM Ti-6Al-4V samples subjected to HIP treatment and showed that surface machining confers higher fatigue resistance to both "as build" and HIPed samples. As explained above, surface roughness and residual stresses are key parameters controlling the fatigue response, making marginal the microstructural effects. Therefore, in order to reduce both the issues derived from undesired surface tensile residual stress and inadequate surface quality, different post-process treatments were proposed and analyzed in the technical literature. Accordingly, two main types of post-process treatments were investigated, the former represented by mechanical treatments as machining (Ackelid and Svensson, 2009; Chastand et al., 2016; Greitemeier et al., 2016; Kasperovich and Hausmann, 2015; Leuders et al., 2013; Rafi et al., 2013; Van Hooreweder et al., 2012; Xu et al., 2015), shot peening (Wycisk et al., 2013) and sand blasting (Gong et al., 2012), the latter consisting in the electrochemical treatment (Baufeld et al., 2011; Brandl et al., 2010, 2011), that, combined with the HIP treatment, confers a fatigue resistance comparable with that of components obtained with traditional manufacturing technologies (Li et al., 2010). Of particular interest in prosthetic implants is the possibility of exploiting the surface morphology to improve the biocompatibility. In this context, surface treatments such as sand-blasting and shot-peening could be applied to obtain a surface texture able to promote the osseointegration (Aparicio et al., 2003; Cho and Park, 2003; Le Guehennec et al., 2008; Ball et al., 2008; Jäger et al., 2007).

1.2 Aim and scopes

The present paper explores the effect of different post-process treatments on the fatigue and biocompatibility performance of specimens produced by AM. Paper's aim is to identify the most appropriate post-sintering treatment for biomedical applications able to improve the fatigue performance and to enhance, or at least not to jeopardize, the cell proliferation on the printed metallic surface. It is in fact widely recognized in the technical literature that surface treatments like electro-polishing and shot peening beneficially impact on the fatigue properties of metallic materials; however, it is still debated how the surface smoothening exerted by the former one and the surface morphology modifications produced by the latter one

influence the biocompatibility of metallic implants (Anselme, 2000; E.M. Lee et al., 2016). For this purpose, cylindrical specimens are printed by selective laser melting of biomedical Titanium Grade 23 powder. After the building process, all samples are heat treated to achieve a complete stress relief. Part of them is tribofinished with the aim of reducing the surface roughness. In addition, some of the tribofinished samples are subject to one of the following post-sintering treatments: (i) shot peening, (ii) hot isostatic pressing (HIP), and (iii) electropolishing. Fully-reversed axial fatigue tests are carried out exploring fatigue lives comprised between 5×10^4 and 5×10^7 cycles. The material characterization is complemented with tensile tests, surface roughness, microhardness and in-depth residual stress profiles measurements. Finally, the biological properties are explored in terms of cell growth on the differently treated surfaces. For this purpose, MG-63 cells, deriving from human bone osteosarcoma, are seeded on cylindrical samples and their growth is analysed.

2. Experimental material and procedures

2.1 Specimens preparation and post-sintering treatments

The specimens are produced using the biomedical Titanium Grade 23, also indicated as Ti-6Al-4V ELI, due to its very low content of interstitial elements, as demonstrated by the nominal chemical composition listed in Table 1.

The alloy is supplied in the form of atomized powder. The near spherical shape of the particles is shown in Fig. 1(a). The particle size distribution shown Fig. 1(b) indicates that the adopted SLS procedure employees a very fine powder with an average diameter of about 9 μm.

Fatigue tests are carried out on cylindrical specimens, whose geometry, compliant with the standard ASTM E606, is shown in Figure 2. Specifically, the samples are provided with a uniform-gage test section. In this way, the critically stressed volume is larger than that in common hourglass specimens, hence the detrimental effect of manufacturing defects, such as internal pores and surface cavities, on the fatigue performances can be more likely revealed. The samples are manufactured by 3DZ (Treviso, Italy) along the longitudinal direction (z-axis) by selective laser melting (SLM), using the 3D Systems ProX 300 printer, whose main technical characteristics are listed in Table 2.

The complete stress relief after SLM is achieved by heat-treating the samples at 670°C for 5 hours in a protective Ar-atmosphere to achieve a complete stress relief. Specimens in this condition will be referred to as "as-built". Part of the specimens is tribofinished using a controlled vibrating tank with an aqueous medium containing high quality granulates and additives (mainly surfactants) with the aim of reducing the surface roughness. Finally, some of the tribofinished samples are subject to one of the following post-sintering treatments: (i) shot peening, (ii) hot isostatic pressing (HIP), and (iii) electropolishing, in order to modify the morphology and the mechanical properties of the surface layer.

Shot peening is applied with the aim of introducing compressive residual stresses and closing porosity on the surface layers, without increasing the surface roughness. For this purpose, several shot peening processes differing in peening medium and intensity have been explored. Among the peening treatments, which proved not to significantly increase the surface roughness with respect to the tribofinished condition, we selected the most intense one, as it can impart more likely high compressive residual stresses and reduce surface porosity. Specifically, medium-size ceramic beads, widely used in the aircraft industry and also compliant with biocompatibility requirements, are propelled by an-air blast machine to a moderately high Almen intensity. The main process parameters are summarized in Table 3.

The HIP treatment is conducted with the aim of increasing the apparent density of the entire sample and to transform the little ductile martensitic microstructure obtained after sintering into lamellar α+β microstructure. Specifically, HIP is carried out at 920 °C, 1000 bar of pressure for 2 hours.

Electropolishing is conducted according to the procedure described by Tajima et al., 2008. They developed an alcoholic solution as alternative to traditional dangerous electrolytes, which can contaminate the implant and have adverse effects on its biocompatibility, ranging from inflammatory reaction due long term contact to high dosage toxicity (Sansone et al., 2013). This solution is composed by ethyl alcohol (700 ml/L), isopropyl alcohol (300 ml/L), aluminium chloride (60 g/L) and zinc chloride (250 g/L). A meshed ring made of platinum is used as cathode and a magnetic anchor is used to agitate the solution. The electropolishing is performed using as electrolytic condition of 70V and 2.0 kA/m^2, and 30°C for 30 minutes, every 10 minute the specimens is rotated by 90° in order to obtain the most homogeneous surface finish. After the electropolishing the cross-section diameter is reduced by about 1mm.

2.2 Mechanical tests

Monotonic tensile tests (initial strain rate of 1×10^{-4} s^{-1}) are performed on cylindrical hourglass specimens in as-built and HIPed conditions on a servo-hydraulic universal testing machine INSTRON 1343, equipped with hydraulic grips, a load cell of 100 kN (nonlinearity ±0.1% of R.O.) and an axial extensometer (10 mm gauge length, nonlinearity ±0.15% of R.O.).

Alternating (zero mean stress, load ratio R=-1) axial fatigue tests are carried out in laboratory environment using a resonant testing machine Rumul Mikrotron 20 kN operating at a nominal frequency of 150 Hz under load control. The load direction is aligned with the z-building axis of the samples. Different stress levels corresponding to fatigue lives in the range between nearly 10^4 and 5×10^7 cycles are explored. Specifically, run-out fatigue tests are terminated at 5×10^7 cycles when no fracture occurs, a relatively long fatigue life intentionally selected in order to investigate fatigue damage phenomena arising only in the very high-cycle fatigue regime.

Two types of fatigue curves are obtained, i.e. without and with knee located around 10^6 fatigue cycles. The former fatigue curves are represented by a S-N curve in the form of:

$$\sigma_a = c_1 \times N_f^{-\frac{1}{c_2}} \tag{1a}$$

The latter fatigue curves are represented by a S-N curve expressed by:

$$\sigma_a = c_1 + \frac{c_2}{N_f^m} \tag{1b}$$

The scatter of the fatigue data is estimated by computing the estimated regression variance assumed to be uniform for the whole fatigue curve and expressed by:

$$S^2 = \frac{\sum_{i=1}^{n}\left(\sigma_{a,i} - \hat{\sigma}_{a,i}\right)^2}{n-p} \tag{2}$$

where $\sigma_{a,i}$ is the i-th fatigue amplitude data point, $\hat{\sigma}_{a,i}$ is its estimator, n is the number of data elements, and p is the number of parameters in the regression; p = 2 and 3 for Eq. (1a) and (1b), respectively.

2.3 Material and specimens characterization

The residual stress analysis is performed by X-ray Diffraction (XRD) technique using an AST X-Stress 3000 X-ray diffractometer. Measurements are made with Cu Kα radiation in both radial and longitudinal

direction in the gage region. The analysis area is limited by a collimator of 1 mm^2 in area. The classical $\sin^2\psi$ method is applied for stress evaluation considering 9 diffraction angles (2θ) scanned between -45° and 45°. High angle measurements (2θ angle 137.0°) with higher strain sensitivity are obtained choosing the <201> diffracting planes. The experiment is conducted after a calibration of the system that was checked by collecting a diffraction pattern from a standard polycrystalline Ti powder. In-depth measurements are done using an electro-polishing incremental layer removal technique, which is arrested when layers subject to tensile residual stresses, i.e. about 150 μm below the surface, are exposed.

Microhardness profiles are measured to characterize the material's work hardening. A diamond Vickers indenter is used applying a maximum force of 1 N. The load is applied at a constant 0.1 N/s rate with a dwell time of 10 s. Three measurements are performed at each depth and averaged in order to account for material's heterogeneity and measurement errors.

Surface roughness is investigated using a contact profilometer, the samples are cut in order to have an easier measurement on the gage length, the instrument is aligned longitudinally with the sample, the scanned length is 4 mm for each sample.

The metallographic analysis is performed on a section of the sample taken from the gage length. After cutting, the sample is mounted, grinded from 220 to 4000 mesh SiC abrasive papers, and polished using a 3-micron diamond paste and a 0.04-micron alumina suspension. A Kroll's etching is used to reveal the microstructures. Porosity is measured on three metallographic samples using image analysis software ImageJ®. Porosity values are expressed in terms of mean value and standard deviation in order to account for material's heterogeneity and measurement errors.

The fracture surfaces and the external sample surfaces are investigated under a JEOL JSM-IT300LV Scanning electron microscope, pictures are taken in both secondary and back-scattered electron, the quantitative chemical analysis is performed by EDXS probe.

2.4 Biological tests

The samples biocompatibility is characterized following the procedure schematized in Fig. 3. Specifically, MG-63 cell line (*Homo sapiens* bone osteosarcoma; ATCC® CRL-1427™) are cultured in Eagle's Minimum Essential Medium (MEME; Sigma-Aldrich) supplemented with 10% fetal bovine serum

(Sigma–Aldrich), 1% L-glutamine (Sigma-Aldrich) and 1% penicillin and streptomycin (Sigma–Aldrich). Cylindrical samples with different treatments are sterilized in autoclave before placing in a 24-well plate. MG-63 cells are seeded at 5 x 10^4 cells/sample in 1 ml of medium, and cultured at 37°C in a humidified atmosphere with 5% CO_2 concentration. Standard titanium disks are subjected to the same protocol in order to have comparison samples.

Cell growth is assessed using the MTT reduction assay. This assay is based on the reduction operated by viable cells via specific enzymes of the MTT dye (3-(4,5-dimethylthiazol-2-yl)-2,5-diphenyltetrazolium bromide, Sigma-Aldrich) to insoluble formazan salts. Briefly, the cell-seeded cylinders are removed at fixed time from the original wells and placed in fresh wells containing 0.5 ml of culture medium and 0.5 ml of a 0.4 mg/ml MTT solution in DPBS (Sigma-Aldrich). After 2 h of incubation, 1 ml of MTT solvent (i.e. 10% SDS in 0.01N HCl) is added to each sample to dissolve the dark blue crystals and cells were cultured for 2 more hours at 37°C and 5% CO_2. Finally, the absorbance at 575 nm is measured using the Jasco V-550 UV-Vis spectrophotometer.

Percentage of cell growth is calculated as follows: cell growth (%) = $(A_s\text{-}A_0)/(A_c\text{-}A_0)$ x 100, where A_s is the absorbance value of the sample, A_c is the absorbance of cells grown on titanium disks (control) and A_0 is the blank value (no cells). All absorbance values are normalized to the sample surface area. For cylindrical samples, the lateral area is considered.

3. Results and discussion

3.1 Microstructure

Figure 4 illustrates the microstructure of the different material conditions. Fig. 4a shows the microstructure after stress relief (viz. “as-built” condition), which is composed of a very fine aciculate α’ martensite produced by the high cooling rate of the SLM process. The successive process steps with the consequent fusion and solidification of the upper layer may promote grain growth of the previous layer but however it is not sufficient to relieve residual stresses or to transform the martensitic microstructure. Once the part is completed, this shows a brittle behavior and a heat treatment is necessary to modify the microstructure or at least relieve residual stresses. Fig. 4b depicts the microstructure of HIPed samples. This heat treatment completely transforms the α’ phase into α+β phase without any grain growth. The final

lamellar microstructure is formed due to the diffusional β → α transformation with lamellas of α phase within a β phase matrix.

Figure 5 illustrates the results of the porosity measurements undertaken in three samples taken from the as-received, tribofinished, shot-peened and HIPed variants. As schematically shown in Fig. 5a for illustrative purpose, the porosity is measured on 4 concentric annular areas in which the samples cross-section has been ideally divided. The results shown in Fig. 5b indicate that the average porosity of the as-received condition is about 0.20%, demonstrating that the SLM treatment proved to confer near full-density. A higher porosity of about 0.35% is detected on the surface layers. The tribofinishing, and, to an even greater extent, the shot-peening treatments are able to reduce the porosity of the outer layers, while they leave the porosity of the underlying layers nearly unchanged. Apart from the innermost zone 1, the HIP treatment produces a more pronounced reduction in porosity with an average value of 0.07%.

3.2 Tensile properties

The monotonic tensile properties are strictly correlated with the microstructural conditions. The properties of the α' martensitic and α+β lamellar microstructures, typical of as-built and HIPed specimens respectively, are summarized in Table 4. The Young's modulus is similar for both microstructures, with a value around 110 GPa. On the other hand, greater difference is observed in terms of yield strength, UTS and total elongation, where the martensitic microstructure exhibits higher yield stress and tensile strength, but lower total elongation, nevertheless compliant with the minimum required elongation for biomedical devices according to the standard ASTM F2924 – 14. These differences in terms of mechanical properties stem from the peculiar characteristics of the two microstructures. High tensile strength is conferred to the metastable α' martensite by the shorter effective slip length compared to the α+β microstructure. The higher elongation as well as the lower yield stress and tensile strength of the HIPed specimens derive from the volume fraction of the more ductile β phase and a greater amount of independent slip planes compared with the α phase.

3.3 Surface morphology

Figure 6 shows the SEM micrographs illustrating the morphology of the outer surface of the samples. Striations along the building direction and unfused particles can be noted on the surface of the as-built

specimen (Fig. 6a). The tribofinishing process (Fig. 6b) produces a surface smoothening accompanied by an intense plastic deformation and rubbing of the unfused powder particles. The electropolished surface (Fig. 6c) is even smoother and characterized by small remnants of unfused particles. Shot peening (Fig. 6d) produces a more homogeneous surface with respect to the initial tribofinished surface and introduces small impact dimples. Finally, the HIP treatment (not shown for the sake of brevity) produces a surface smoothening similar to the shot peened ones but with no evidence of surface dimples.

The SEM observations are consistent with the results of the roughness measurements listed in Table 5. As expected, the as-built variant displays the greatest roughness value. Nevertheless, a R_a roughness value of about 7 μm can be considered fairly low for this kind of manufacturing technology and has been achieved owing to the very fine powder size employed by the SLM process. A drastic drop in roughness is obtained through electropolishing. The remaining post-process conditions exhibit intermediate roughness values. It is worth noting that the selected shot peening treatment is even able to reduce the surface roughness of the starting tribofinished surface condition.

3.4 Microhardness

The microhardness is an indirect measure of the ductility of the material microstructure and the work hardening introduced into the material by the post-sintering treatments. Figure 7 compares the microhardness profiles of the as-built, tribofinished, shot-peened and HIPed specimens. The microhardness values of the as-built condition can be taken as the reference value for all the conditions presenting a martensitic α' microstructure. The average reference microhardness is about 380 HV with a standard deviation of 10 HV. The strain hardening introduced by tribofinishing and shot-peening processes increases the hardness of the surface layers, over a depth below the surface varying between 0.15 and 0.30 mm, respectively. The HIPed condition displays lower microhardness values due to the softer α+β microstructure. The large surface microhardness can be explained by the intense plastic deformation produced by the thermo-mechanical treatment on the surface layers.

3.5 Residual stresses

Different residual stresses are introduced into the specimens by some of the post-sintering treatments through the plastic deformation of the material. Figure 8 shows the in-depth profiles of hoop and axial residual stresses for the as-built, tribofinished, HIPed, and shot-peened conditions. Residual stresses are quite low in the as-built specimen. The stress relief treatment is thus effective in nearly completely eliminating the high residual stresses expected after sintering (Fergani et al., 2017); only in the axial direction a small tensile stress is present. Tribofinished, HIPed and shot-peened specimens display near the surface (axial and hoop) compressive residual stresses that decrease moving towards the specimen interior. The highest compressive stresses are displayed by the shot-peened condition. Specifically, the axial and hoop stresses show a sub-superficial peak of -800 MPa and -700 MPa, respectively, located at a depth of about 30 μm below the surface. The thickness of the layer interested by compressive residual stresses is about 0.15 mm; this effective treatment depth is in fairly good agreement with that estimated from the microhardness measurements The tribofinished condition shows a superficial peak of both axial and hoop components of about -400 MPa, that quickly decreases until becoming nearly zero 0.1 mm below the surface. Finally, the surface of the HIPed condition is not affected by tensile residual stresses but display remarkable hoop and axial stresses compressive of -450 MPa. This could be associated with the intense work-hardening of the surface layers attested by the micro-hardness measurements.

3.6 Fatigue curves

The results of the fatigue tests as well as the fitting curves (corresponding to 50% failure probability) are compared in Fig 9. The best-fit parameters representing the fatigue curves, according to Eqs. (1), are listed in Table 6, which reports also the standard deviation S calculated as the root square of the estimated regression variance S^2.The fatigue curves of the as-built, tribofinished, electropolished and HIPed conditions are well represented by Eq. (1b) showing a knee around 1×10^6 cycles. On the contrary, the fatigue curve of the peened condition steadily declines with the fatigue life. It is then well represented by the linear relation in double-logarithmic scale represented by Eq. (1a), and show occurrence of failure throughout the explored fatigue life interval. A similar behavior has been observed in shot-peened samples of Al-7075-T651 (Benedetti et al., 2016).

At first glance, it can be noted from Fig. 9 and Table 6 that the fatigue resistance of the as-built condition is pretty low, in fact the high-cycle fatigue is about 220 MPa at 50 millions cycles, i.e. more than 50% lower than hat reported in the technical literature (Lütjering and Williams, 2007) for forged Ti-6Al-4V. The scatter in fatigue data is also remarkable, being about 10% of the high-cycle fatigue resistance.

The electropolished samples show an improvement in the fatigue behavior, namely the fatigue resistance at the same lifetime increases by 14% up to 250 MPa and the scatter is reduced by 30%. This gives an idea about how the surface roughness impacts on the fatigue performance, nonetheless the improvement produced by roughness smoothing is quite limited if compared with that achieved by the remaining post-sintering processes.

For instance, the tribofinished condition imparts an increment in high-cycle fatigue strength up to 340 MPa, even though without any reduction in fatigue scatter. This suggests that introducing surface compressive residual stresses has a more beneficial effect than reducing surface roughness. Apparently, compressive residual stresses hinder crack initiation and propagation in the surface layers affected by the treatments. This is also demonstrated by the fatigue performance of the HIPed condition, which displays the highest fatigue endurance equal to 370 MPa and diminishes the fatigue scatter by about 15%. In this case, beside introducing surface compressive residual stresses (comparable to those introduced by tribofinishing), the HIP treatment reduces sintering-induced defects through fusion of unmolten particles and reduction in residual porosity. Moreover the thermal treatment produces a more ductile microstructure that can help attenuate local peak stresses due to stress redistribution in the vicinity of defects. Very interesting is the fatigue behavior of the shot peened condition. It displays the highest fatigue resistance in the low-to-medium cycle fatigue regimes, a decrease in fatigue scatter comparable to HIP, and steadily declining fatigue strength with increasing fatigue lifetimes. Therefore, in the very high-cycle fatigue regime its fatigue resistance is slightly lower (340 MPa) than that of the HIPed condition. This suggests that the high residual stresses introduced by shot peening is more effective in hindering fatigue crack initiation and propagation in the low-to-medium than in the very-high cycle fatigue regime. Further discussion of the fatigue results is provided in the next section.

3.7 Fatigue fracture surfaces and discussion of the fatigue results

The fracture surfaces of the fatigued specimens are investigated by SEM. Figure 10 shows the failure types detected for the different conditions. Figure 10a illustrates the typical fracture surface of the as-built condition. The point of crack initiation, highlighted with the red arrow, is a pore at or in the vicinity of the surface and, in its neighborhoods, others defects working as promoters of the crack propagation can be observed. Also the fracture surface of tribofinished samples indicates crack initiated at surface defects. Indeed, Figure 10b shows surface voids, which caused stress concentration that promoted the early stages of crack propagation. Figure 10c illustrates the fracture surface of an electropolished sample: also in this case the site of crack nucleation is a superficial pore. The limited fatigue improvement conferred by electropolishing can therefore be explained by the removal of surface layers which exposes on the polished surface internal pores and at the same time eliminates the beneficial compressive residual stresses introduced by tribofinishing. Apparently, roughness smoothening can only barely overweigh these two detrimental effects.

Figure 10d shows the fracture surface of a HIPed sample; in this case the crack initiation site is located on a shallow crater. This surface defect as in the case of tribofinished sample causes strain localization during the early stages of crack propagation. Moreover the extension of the plastically deformed area is greater than the other cases probably due to the more ductile phase that characterized these samples. It can be also noticed that the fracture surface displays fewer defects and pores that might constitute preferential paths for crack propagation. Figure 10e illustrates a fracture surface typically observed in shot-peened samples. Unlike the remaining conditions, the crack initiation site is located well below the surface and in the vicinity of an internal pore. The different location of the critical defects can be explained invoking the high compressive surface residual stresses that suppress surface crack initiation and push it below the layer affected by the shot peening treatment. This has been commonly observed in samples tested in the very high-cycle fatigue regime (Atrens et al., 1983; Gilbert and Piehler, 1993; Ravi Chandran and Jha, 2005), especially in the presence of compressive surface residual stresses (Benedetti et al., 2015). In this specific case, the cracks initiated at pores located in sub-superficial layers not reached by the effects of the surface treatment are invariably destined to propagate up to the surface thus leading to the eventual fracture, especially in the very-high cycle fatigue regime. This damage mechanism along with residual stress evolution during the fatigue life can

explain the progressive decline in the fatigue strength gain displayed by the peened samples with increasing fatigue lifetime.

In conclusion, Table 7 summarizes all the possible factors that can influence the very high (VHC, 50×10^6) and high (HC, 5×10^6) cycle fatigue resistance of the conditions investigated in the present paper. It can be noticed that tribofinished and HIPed conditions have the same HC fatigue resistance and comparable surface roughness and compressive residual stresses. This suggests that the relieved martensitic and the lamellar microstructures produce a similar HC fatigue strength and that the higher VHC fatigue resistance of the HIPed condition can be due to the reduced porosity and consequently lower likelihood of critical defects. Eliminating surface roughness by electropolishing is more effective on the HC, less in the VHC fatigue regime, presumably because this beneficial effect is partly lost due to the exposure of internal pores on the polished surface. Finally, the HC fatigue resistance greatly benefits from compressive residual stresses and porosity reduction induced in the surface layers by shot peening, but these beneficial effects are partly counterbalanced in the VCF regime by the presence of sub-superficial pores, which can be eliminated or reduced only by the HIP treatment.

3.8 Biological properties and final discussion

A specific aim of the present paper is to investigate if the surface treatments investigated so far can affect the biological properties of the samples. For this purpose, the analysis is focused on the two surface treatments that most changed the surface morphology of the as-built specimens, viz. shot peening that introduces a pattern of surface dimples and electropolishing that nearly completely eliminates the surface roughness. Specifically, the biological properties are investigated in terms of cell growth at different times. Cell proliferation is evaluated with the MTT assay, which is based on the conversion of the yellowish MTT solution to dark blue, water-insoluble MTT formazan crystals, by mitochondrial dehydrogenases of living cells. Since only living cells can process MTT, this assay can be used to measure the cell growth on different surfaces. The absorbance values deriving from this assay are normalized to the lateral area of cylindrical samples and referred to a titanium disk sample, arbitrary selected as a control. Titanium either pure or alloy (Shah et al. 2016) or even as nanostructured material (Kulkarni et al. 2015) show indeed excellent properties both in term of corrosion resistance and biocompatibility. These excellent properties are shown also by the

titanium disks samples tested in this paper and therefore these samples are selected as positive control. The cell growth values obtained with these non-treated samples are considered as the maximum growth values (i.e. 100%) to which all data are referred.

As shown in Fig. 11, cell growth on the treated samples seems quite low with respect to the titanium disk sample (100%), but this result is easily explained considering that cells seeded on flat samples better adhere to the surface and therefore are present in a bigger number since the beginning of incubation. This phenomenon is particularly evident for short-term incubations, such as 24 h (Figure 11), while the gap between cylindrical and flat samples tends to reduce increasing the time of incubation (66 and 90 h of incubation, Figure 8) and is expected to disappear for longer incubations, i.e. 14-21 days (Ryan et al. 2008). Cell growth on controls is therefore higher than on cylindrical samples, as expected.

The shape effect described above is negligible for the cylindrical samples, which have similar shape and dimensions. A direct comparison among the three types of samples is therefore possible. No significant differences are visible in terms of cell growth at different times, suggesting that post-sintering treatments which could improve titanium mechanical properties do not significantly affect the biological properties of these materials. It is indeed well known that several surface aspects influence osteoblasts adhesion on materials, for example topography, chemistry or surface energy (Anselme, Biomaterials 2000). Regarding topography, scanning electron microscopic analysis of bone cells on materials with various surface morphologies generally demonstrated that cell spreading and continuous cell layer formation is better on smooth surfaces compared to rough ones. However, it is also demonstrated that microrough Ti and Ti alloy surfaces promote osteoblastic differentiation of cells at the expense of attachment and proliferation (E.M. Lee et al. Biomaterials 2016). Accordingly, our samples that have different surface roughness (Table 5), show a quite similar behavior regarding cell growth and proliferation.

In conclusion, the good biocompatibility of the starting material is preserved after the surface treatments. The selection of the more suitable surface treatment is then driven by other considerations, like the allowable fatigue strength of the implant or the cost and duration of the post-sintering treatment. To this regard, the shot peening treatment may be the preferred choice if the implant is designed to operate in the medium-to-high cycle fatigue regime and low treatment costs are required. Conversely, the HIP treatment provides the highest very-high-cycle fatigue strength, but at higher costs.

4. Conclusions

The fatigue behavior of plane samples manufactured by SLM has been experimentally investigated exploring fatigue lives comprised between nearly 10^4 and 5×10^7 cycles. Several post-sintering treatments have been explored with the aim of improving the fatigue resistance. The following conclusions can be drawn:

1) Introducing surface compressive residual stresses and reducing porosity are the most effective ways to improve the fatigue resistance of SLM parts. In fact, HIP, shot peening and tribofinishing proved to confer the highest increments in fatigue strength.
2) Eliminating surface roughness by electropolishing produces a limited increment in the fatigue resistance, since sub-surface pores are exposed to the polished surface so as they can act as crack initiation sites.
3) In the very high cycle fatigue regime, fatigue cracks tend to initiate preferentially in the vicinity of sub-superficial defects. Therefore, the highest increment in fatigue strength in this regime was obtained by HIP, which is able to close porosity over the entire cross-section. Conversely, shot peening reduces porosity only in the surface layers, thus resulting less effective at very long fatigue lifetimes.
4) The good biocompability of the starting material is not significantly affected by the surface treatments. Their selection is then driven by different considerations. The shot peening treatment may be the preferred choice if the implant is designed to operate in the medium-to-high cycle fatigue regime and low treatment costs are required. Contrariwise, the HIP treatment provides the highest very-high-cycle fatigue strength, but at higher costs.

Acknowledgments

This work was financially supported by the University of Trento, within the strategic research project 2014 (under grant P.STR.14 3D) entitled “3D printed metallic foams for biomedical applications: understanding and improving their mechanical behavior”.

References

Ackelid, U., Svensson, M., 2009. Additive Manufacturing of Dense Metal Parts by Electron Beam Melting. Mater. Sci. Technol. Conf. 2711–2719.

Agarwala, M., Bourell, D., Beaman, J., Marcus, H., Barlow, J., 1995. Post-processing of selective laser sintered metal parts. Rapid Prototyp. J. 1, 36–44.

Anselme, K., 2000. Osteoblast adhesion on biomaterials. Biomaterials 21, 667-681

Aparicio, C., Gil, F.J., Fonseca, C., Barbosa, M., Planell, J.A., 2003. Corrosion behaviour of commercially pure titanium shot blasted with different materials and sizes of shot particles for dental implant applications. Biomaterials 24, 263–273.

Atrens, A., Hoffelner, W., Duerig, T.W., Allison, J.E., 1983. Subsurface crack initiation in high cycle fatigue in Ti6A14V and in a typical martensitic stainless steel. Scr. Metall. 17, 601–606. doi:10.1016/0036-9748(83)90385-X

Bagno, A., Di Bello, C., 2004. Surface treatments and roughness properties of Ti-based biomaterials. J. Mater. Sci. Mater. Med. 15, 935–949.

Ball, M., Grant, D.M., Lo, W.-J., Scotchford, C.A., 2008. The effect of different surface morphology and roughness on osteoblast-like cells. J. Biomed. Mater. Res. A 86A, 637–647. doi:10.1002/jbm.a.31652

Barriuso, S., Chao, J., Jiménez, J.A., García, S., González-Carrasco, J.L., 2014. Fatigue behavior of Ti6Al4V and 316 LVM blasted with ceramic particles of interest for medical devices. J. Mech. Behav. Biomed. Mater. 30, 30–40.

Baufeld, B., Brandl, E., Van der Biest, O., 2011. Wire based additive layer manufacturing: comparison of microstructure and mechanical properties of Ti–6Al–4V components fabricated by laser-beam deposition and shaped metal deposition. J. Mater. Process. Technol. 211, 1146–1158.

Benedetti, M., Fontanari, V.. The effect of bi-modal and lamellar microstructures of Ti-6Al-4V on the behaviour of fatigue cracks emanating from edge-notches. 2004. Fatigue Fract Engng Mater Struct 27, 1073–1089.

Benedetti, M., Heidemann, J., Peters, J.O., Lütjering G. 2005. Influence of sharp microstructural gradients on the fatigue crack growth resistance of α + β and near-α titanium alloys. Fatigue Fract Engng Mater Struct 28, 909–922.

Benedetti, M., Fontanari, V., Bandini, M., Savio, E., 2015. High- and very high-cycle plain fatigue resistance of shot peened high-strength aluminum alloys: the role of surface morphology. Int J Fatigue 70, 451–62. L SEP

Benedetti, M., Fontanari, V., Allahkarami, M., Hanan, J.C., Bandini, M., 2016. On the combination of the critical distance theory with a multiaxial fatigue criterion for predicting the fatigue strength of notched and plain shot-peened parts. Int. J. Fatigue 98, 133-147.

Brandl, E., Baufeld, B., Leyens, C., Gault, R., 2010. Additive manufactured Ti-6Al-4V using welding wire: comparison of laser and arc beam deposition and evaluation with respect to aerospace material specifications. Phys. Procedia 5, 595–606.

Brandl, E., Heckenberger, U., Holzinger, V., Buchbinder, D., 2012. Additive manufactured AlSi10Mg samples using Selective Laser Melting (SLM): Microstructure, high cycle fatigue, and fracture behavior. Mater. Des. 34, 159–169.

Brandl, E., Leyens, C., Palm, F., 2011. Mechanical properties of additive manufactured Ti-6Al-4V using wire and powder based processes, in: IOP Conference Series: Materials Science and Engineering. IOP Publishing, p. 012004.

Campoli, G., Borleffs, M.S., Yavari, S.A., Wauthle, R., Weinans, H., Zadpoor, A.A., 2013. Mechanical properties of open-cell metallic biomaterials manufactured using additive manufacturing. Mater. Des. 49, 957–965.

Chastand, V., Tezenas, A., Cadoret, Y., Quaegebeur, P., Maia, W., Charkaluk, E., 2016. Fatigue characterization of Titanium Ti-6Al-4V samples produced by Additive Manufacturing. Procedia Struct. Integr. 2, 3168–3176.

Cho, S.-A., Park, K.-T., 2003. The removal torque of titanium screw inserted in rabbit tibia treated by dual acid etching. Biomaterials 24, 3611–3617.

Collins, P.C., Haden, C.V., Ghamarian, I., Hayes, B.J., Ales, T., Penso, G., Dixit, V., Harlow, G., 2014. Progress Toward an Integration of Process–Structure–Property–Performance Models for "Three-Dimensional (3-D) Printing" of Titanium Alloys. JOM 66, 1299–1309.

Facchini, L., Magalini, E., Robotti, P., Molinari, A., 2009. Microstructure and mechanical properties of Ti-6Al-4V produced by electron beam melting of pre-alloyed powders. Rapid Prototyp. J. 15, 171–178.

Facchini, L., Magalini, E., Robotti, P., Molinari, A., Höges, S., Wissenbach, K., 2010. Ductility of a Ti-6Al-4V alloy produced by selective laser melting of prealloyed powders. Rapid Prototyp. J. 16, 450–459.

Fergani, O., Berto, F., Welo T., Liang, S.Y., 2017. Analytical modelling of residual stress in additive manufacturing. Fatigue&Fracture of Engineering Materials & Structures. doi: 10.1111/ffe.12560

Frazier, W.E., 2014. Metal additive manufacturing: a review. J. Mater. Eng. Perform. 23, 1917–1928.

Froes, F.H., Dutta, B., 2014. The Additive Manufacturing (AM) of Titanium Alloys, in: Advanced Materials Research. Trans Tech Publ, pp. 19–25.

Gilbert, J.L., Piehler, H.R., 1993. On the nature and crystallographic orientation of subsurface cracks in high cycle fatigue of Ti-6Al-4V. Metall. Trans. A 24, 669–680.

Goldberg, J.R., Gilbert, J.L., 2004. The electrochemical and mechanical behavior of passivated and TiN/AlN-coated CoCrMo and Ti6Al4V alloys. Biomaterials 25, 851–864. doi:10.1016/S0142-9612(03)00606-9

Gong, H., Rafi, K., Starr, T., Stucker, B., 2012. Effect of defects on fatigue tests of as-built Ti-6Al-4V parts fabricated by selective laser melting, in: Proceedings of the Solid Freeform Fabrication Symposium, Austin, TX, USA. pp. 6–8.

Gorny, B., Niendorf, T., Lackmann, J., Thoene, M., Troester, T., Maier, H.J., 2011. In situ characterization of the deformation and failure behavior of non-stochastic porous structures processed by selective laser melting. Mater. Sci. Eng. A 528, 7962–7967.

Greitemeier, D., Palm, F., Syassen, F., Melz, T., 2016. Fatigue performance of additive manufactured TiAl6V4 using electron and laser beam melting. Int. J. Fatigue.

Hedayati, R., Hosseini-Toudeshky, H., Sadighi, M., Mohammadi-Aghdam, M., Zadpoor, A.A., 2016. Computational prediction of the fatigue behavior of additively manufactured porous metallic biomaterials. Int. J. Fatigue 84, 67–79.

Jäger, M., Zilkens, C., Zanger, K., Krauspe, R., 2007. Significance of nano-and microtopography for cell-surface interactions in orthopaedic implants. BioMed Res. Int. 2007.

Kasperovich, G., Hausmann, J., 2015. Improvement of fatigue resistance and ductility of TiAl6V4 processed by selective laser melting. J. Mater. Process. Technol. 220, 202–214.

Kruth, J.-P., Mercelis, P., Van Vaerenbergh, J., Froyen, L., Rombouts, M., 2005. Binding mechanisms in selective laser sintering and selective laser melting. Rapid Prototyp. J. 11, 26–36.

Kulkarni M., Mazare A., Gongadze E., Perutkova Š ., Kralj-Iglič V., Milošev I., Schmuki P., Iglič A., Mozetič M., 2015. Titanium nanostructures for biomedical applications. Nanotechnology 26, 062002 (18pp)

Lee E.M., Kathryn Smith, Ken Gall, Barbara D. Boyan, Zvi Schwartz, 2016. Change in surface roughness by dynamic shape-memory acrylate networks enhances osteoblast differentiation. Biomaterials 110, 34-44

Le Guehennec, L., Lopez-Heredia, M.-A., Enkel, B., Weiss, P., Amouriq, Y., Layrolle, P., 2008. Osteoblastic cell behaviour on different titanium implant surfaces. Acta Biomater. 4, 535–543.

Leuders, S., Thöne, M., Riemer, A., Niendorf, T., Tröster, T., Richard, H.A., Maier, H.J., 2013. On the mechanical behaviour of titanium alloy TiAl6V4 manufactured by selective laser melting: Fatigue resistance and crack growth performance. Int. J. Fatigue 48, 300–307.

Levy, G.N., 2010. The role and future of the laser technology in the additive manufacturing environment. Phys. Procedia 5, 65–80.

Li, F., Pan, J., Guillon, O., Cocks, A., 2010. Predicting sintering deformation of ceramic film constrained by rigid substrate using anisotropic constitutive law. Acta Mater. 58, 5980–5988.

Lipinski, P., Barbas, A., Bonnet, A.-S., 2013. Fatigue behavior of thin-walled grade 2 titanium samples processed by selective laser melting. Application to life prediction of porous titanium implants. J. Mech. Behav. Biomed. Mater. 28, 274–290.

Lütjering, G., Williams, J.C. 2007. Titanium. 2nd edition. Springer Verlag, Berlin (Germany).

Murr, L.E., Gaytan, S.M., Ceylan, A., Martinez, E., Martinez, J.L., Hernandez, D.H., Machado, B.I., Ramirez, D.A., Medina, F., Collins, S., others, 2010. Characterization of titanium aluminide alloy components fabricated by additive manufacturing using electron beam melting. Acta Mater. 58, 1887–1894.

Murr, L.E., Gaytan, S.M., Medina, F., Lopez, H., Martinez, E., Machado, B.I., Hernandez, D.H., Martinez, L., Lopez, M.I., Wicker, R.B., others, 2010. Next-generation biomedical implants using additive manufacturing of complex, cellular and functional mesh arrays. Philos. Trans. R. Soc. Lond. Math. Phys. Eng. Sci. 368, 1999–2032.

Murr, L.E., Gaytan, S.M., Ramirez, D.A., Martinez, E., Hernandez, J., Amato, K.N., Shindo, P.W., Medina, F.R., Wicker, R.B., 2012. Metal fabrication by additive manufacturing using laser and electron beam melting technologies. J. Mater. Sci. Technol. 28, 1–14.

Murr, L.E., Quinones, S.A., Gaytan, S.M., Lopez, M.I., Rodela, A., Martinez, E.Y., Hernandez, D.H., Martinez, E., Medina, F., Wicker, R.B., 2009. Microstructure and mechanical behavior of Ti–6Al–4V produced by rapid-layer manufacturing, for biomedical applications. J. Mech. Behav. Biomed. Mater. 2, 20–32.

Parthasarathy, J., Starly, B., Raman, S., Christensen, A., 2010. Mechanical evaluation of porous titanium (Ti6Al4V) structures with electron beam melting (EBM). J. Mech. Behav. Biomed. Mater. 3, 249–259. doi:10.1016/j.jmbbm.2009.10.006

Pederson, R., 2002. Microstructure and Phase transformation of Ti-6Al-4V. Licentiate Thesis, Luleå University, Sweden.

Qiu, C., Adkins, N.J., Attallah, M.M., 2013. Microstructure and tensile properties of selectively laser-melted and of HIPed laser-melted Ti–6Al–4V. Mater. Sci. Eng. A 578, 230–239.

Park, JB, Lakes, RS. Biomaterials - An introduction, 2nd edn. New York, London: Plenum Press, 1992.

Rafi, H.K., Starr, T.L., Stucker, B.E., 2013. A comparison of the tensile, fatigue, and fracture behavior of Ti–6Al–4V and 15-5 PH stainless steel parts made by selective laser melting. Int. J. Adv. Manuf. Technol. 69, 1299–1309.

Ravi Chandran, K.S., Jha, S.K., 2005. Duality of the S–N fatigue curve caused by competing failure modes in a titanium alloy and the role of Poisson defect statistics. Acta Mater. 53, 1867–1881. doi:10.1016/j.actamat.2004.12.032

Ryan, G.E., A. S. Pandit, D. P. Apatsidis, 2008. Porous titanium scaffolds fabricated using a rapid prototyping and powder metallurgy technique. Biomaterials 29, 3625–3635

Sansone, V., Pagani, D., Melato, M., 2013. The effects on bone cells of metal ions released from orthopaedic implants. A review. Clin. Cases Miner. Bone Metab. 10, 34–40. doi:10.11138/ccmbm/2013.10.1.034

Santos, E.C., Osakada, K., Shiomi, M., Kitamura, Y., Abe, F., 2004. Microstructure and mechanical properties of pure titanium models fabricated by selective laser melting. Proc. Inst. Mech. Eng. Part C J. Mech. Eng. Sci. 218, 711–719.

Sercombe, T., Jones, N., Day, R., Kop, A., 2008. Heat treatment of Ti-6Al-7Nb components produced by selective laser melting. Rapid Prototyp. J. 14, 300–304.

Shah, F.A., Trobos M., Thomsen P., Palmquist A., 2016. Commercially pure titanium (cp-Ti) versus titanium alloy (Ti6Al4V) materials as bone anchored implants — Is one truly better than the other? Materials Science and Engineering C 62, 960–966

Spierings, A.B., Starr, T.L., Wegener, K., 2013. Fatigue performance of additive manufactured metallic parts. Rapid Prototyp. J. 19, 88–94.

Su, X., Yang, Y., Peng, Y.U., Sun, J., 2012. Development of porous medical implant scaffolds via laser additive manufacturing. Trans. Nonferrous Met. Soc. China 22, s181–s187.

Tajima, K., Hironaka, M., Chen, K.-K., Nagamatsu, Y., Kakigawa, H., Kozono, Y., 2008. Electropolishing of CP titanium and its alloys in an alcoholic solution-based electrolyte. Dent. Mater. J. 27, 258–265.

Van Hooreweder, B., Boonen, R., Moens, D., Kruth, J.-P., Sas, P., 2012. On the determination of fatigue properties of Ti6Al4V produced by selective laser melting, in: Structures, Structural Dynamics, and Materials and Co-Located Conferences 53rd Aiaa/Asme/Asce/Ahs/Asc. American Institute of Aeronautics and Astronautics.

Vilaro, T., Colin, C., Bartout, J.-D., 2011. As-fabricated and heat-treated microstructures of the Ti-6Al-4V alloy processed by selective laser melting. Metall. Mater. Trans. A 42, 3190–3199.

Vilaro, T., Colin, C., Bartout, J.-D., Nazé, L., Sennour, M., 2012. Microstructural and mechanical approaches of the selective laser melting process applied to a nickel-base superalloy. Mater. Sci. Eng. A 534, 446–451.

Williams, D.F., 2008. On the mechanisms of biocompatibility. Biomaterials 29, 2941–2953. doi:10.1016/j.biomaterials.2008.04.023

Wise, D.L., 2000. Biomaterials Engineering and Devices. Humana Press, Berlin.

Wycisk, E., Emmelmann, C., Siddique, S., Walther, F., 2013. High Cycle Fatigue (HCF) Performance of Ti-6Al-4V Alloy Processed by Selective Laser Melting. Adv. Mater. Res. 816–817, 134–139. doi:10.4028/www.scientific.net/AMR.816-817.134

Xu, W., Sun, S., Elambasseril, J., Liu, Q., Brandt, M., Qian, M., 2015. Ti-6Al-4V additively manufactured by selective laser melting with superior mechanical properties. JOM 67, 668–673.

Yu, J., Rombouts, M., Maes, G., Motmans, F., 2012. Material properties of Ti6Al4V parts produced by laser metal deposition. Phys. Procedia 39, 416–424.

Table captions

Table

Table 1.

Ti	Al	V	O	N	C	H	Fe
Bal.	5.5-6.75	3.5-4.5	<0.13	<0.05	<0.08	<0.012	<0.25

Table 2.

Laser	500 W/Fiber laser / 1070 nm wavelength
Layer thickness	10÷50 μm
Build envelope capacity	250×250×300 mm
Repeatibility	x = 20 μm, y = 20 μm, z = 20 μm
Minimum detail resolution	x = 100 μm, y = 100 μm, z = 20 μm

Table 3.

Treatment	Bead size (µm)	Bead hardness (HV_1)	Bead composition	Almen intensity	Angle of impingement	Coverage (%)
Z300	300÷425	700	ZrO_2 67% SiO_2 31%	6.4 A	90°	200

Table 4.

Condition	E (GPa)	$\sigma_{Y0.2}$ (MPa)	UTS (MPa)	T.E. (%)
As-built	113	1015	1090	10
HIPed	110	850	960	14

E: Young's modulus, $\sigma_{Y0.2}$: 0.2% yield stress; UTS: ultimate tensile strength; T.E.: total elongation.

Table 5.

Condition	R_a (µm)	R_z (µm)	R_{max} (µm)
As-built	6.83	38.40	43.85
Tribofinished	4.96	28.10	35.20
Electropolished	0.54	2.66	4.41
HIPed	5.07	28.10	35.50
Shot peened	3.36	16.48	20.05

Table 6.

Condition	Equation	c_1 (MPa)	c_2	m	S (MPa)
As-built	(1b)	221	123927	0.646	24.2
Tribofinished	(1b)	343	72061	0.573	25.7
Electropolished	(1b)	242	8706	0.376	17.0
HIPed	(1b)	369	2.30018×10^6	0.897	20.9
Shot peened	(1a)	1315	13.1	-	19.4

Table 7.

Condition	Fatigue resistance (MPa)		Porosity		Surface Hardness	Micro structure	Compressive residual stresses	Roughness
	5×10^6	50×10^6	Surface	Interior				
As-built	240	230	-	-	-	α’	-	-
Tribofinished	380	340	↓	-	-	α’	↑	↓
Electro-polished	300	250	↑	-	-	α’	-	↓↓
HIPed	380	370	↓↓	↓	↓	α+β	↑	↓
Shot peened	480	340	↓	-	↑	α’	↑↑	↓

Figure captions

Fig. 1. (a) SEM micrograph of powder and (b) size distribution.

Fig. 2. Sample geometry used for push-pull fatigue tests (standard ASTM E606). Dimensions are in mm.

Fig. 3. Sketch of the cell growth protocol. MG-63 cells are seeded on titanium samples placed in a 24 wells microplate at 50.000 cells/sample and incubated for different periods of time at 37°C, 5% CO_2 in humidified atmosphere. At desired time, samples are moved to new wells, where MTT is added. After two more hours of incubation, the MTT solvent is added and made to react for 2 hours. Finally, the absorbance of each sample solution is measured.

Fig. 4. Light optical micrographs of the microstructure of the Ti6Al4V ELI SLM sample in the as-received condition (a), after the HIP treatment (b).

Fig. 5. Porosity of the samples. (a) Annular areas in which the cross-section is divided. The image is obtained by collating several optical micrographs (b) Results of the porosity measurements.

Fig. 6. SEM micrographs illustrating the surface morphology of the samples. (a) as-built, (b) tribofinished, (c) electropolished, (d) shot peened.

Fig. 7. Microhardness profiles, obtained by averaging the results of three tests.

Fig. 8. Residual stress profiles measured by XRD technique.

Fig. 9. Stress vs number of cycles to failure (S-N) curves of the investigated sample conditions.

Fig. 10. SEM micrographs of the fracture surfaces around the fatigue crack initiation sites. (a) as-built (250 MPa – 1.31 10^5 cycles) sample, (b) tribofinished (400 MPa – 3.06 10^5 cycles) sample, (c) electropolished (400 MPa – 3.6 10^4 cycles) sample, (d) HIP (425 MPa – 9.95 10^4 cycles) sample, (e) shot-peened (350 MPa – 29 10^6 cycles) sample.

Fig. 11. MG-63 growth at different times of incubation on the differently-finished cylindrical samples. Percentages are calculated with respect to cell grown on standard titanium disks. Mean of at least 4 independent measures and standard errors are shown.

Figures

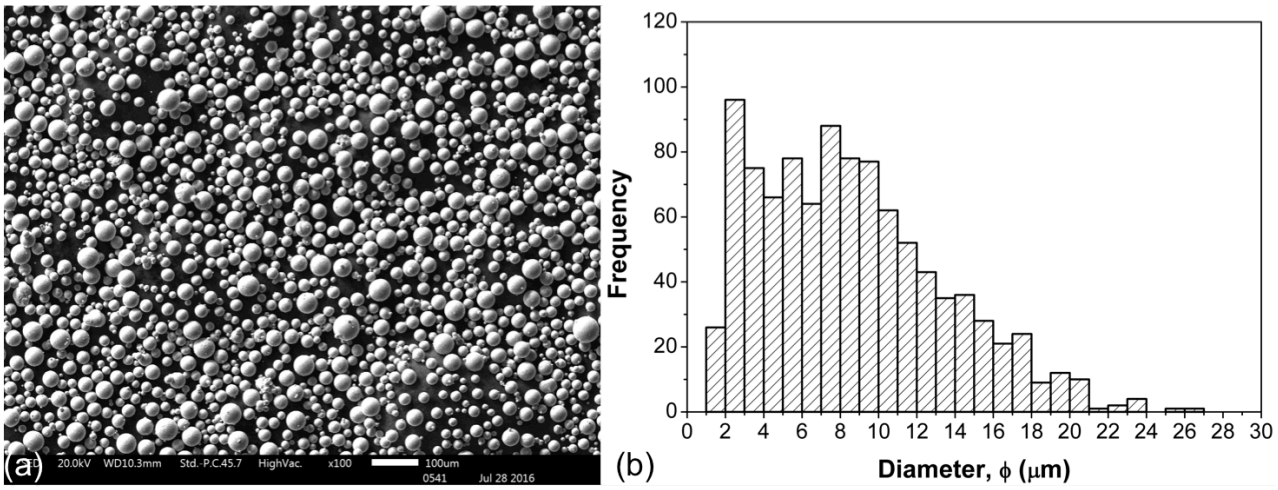

Fig. 1

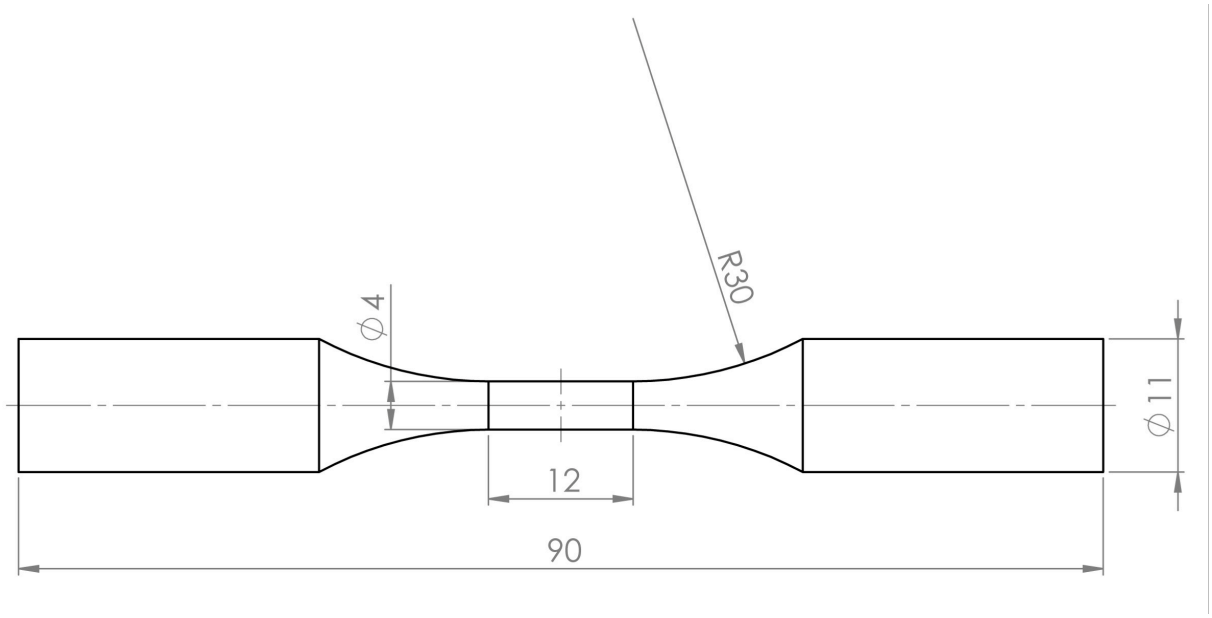

Fig. 2

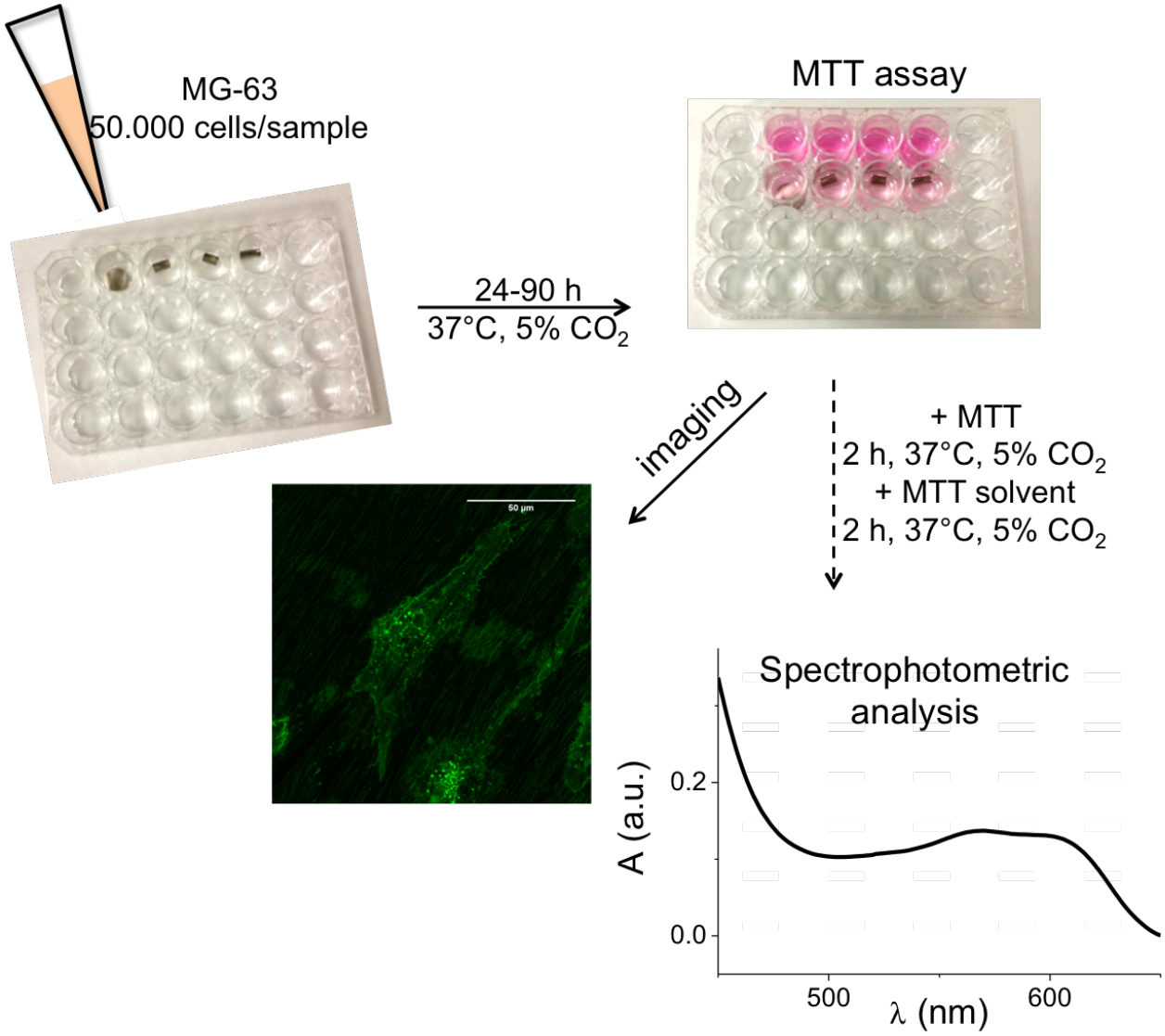
MG-63
50.000 cells/sample
24-90 h
37°C, 5% CO2
MTT assay
imaging
+ MTT
2 h, 37°C, 5% CO2
+ MTT solvent
2 h, 37°C, 5% CO2
50 µm
Spectrophotometric analysis
A (a.u.)
0.2
0.0
500
600
λ (nm)

Fig. 3

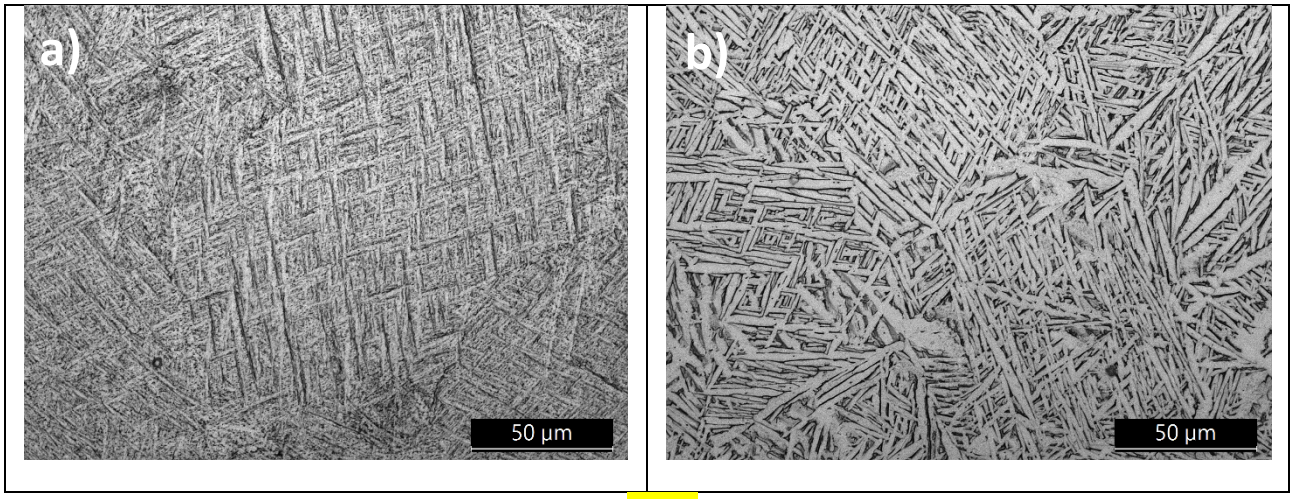
a)
50 µm
b)
50 µm

Fig. 4

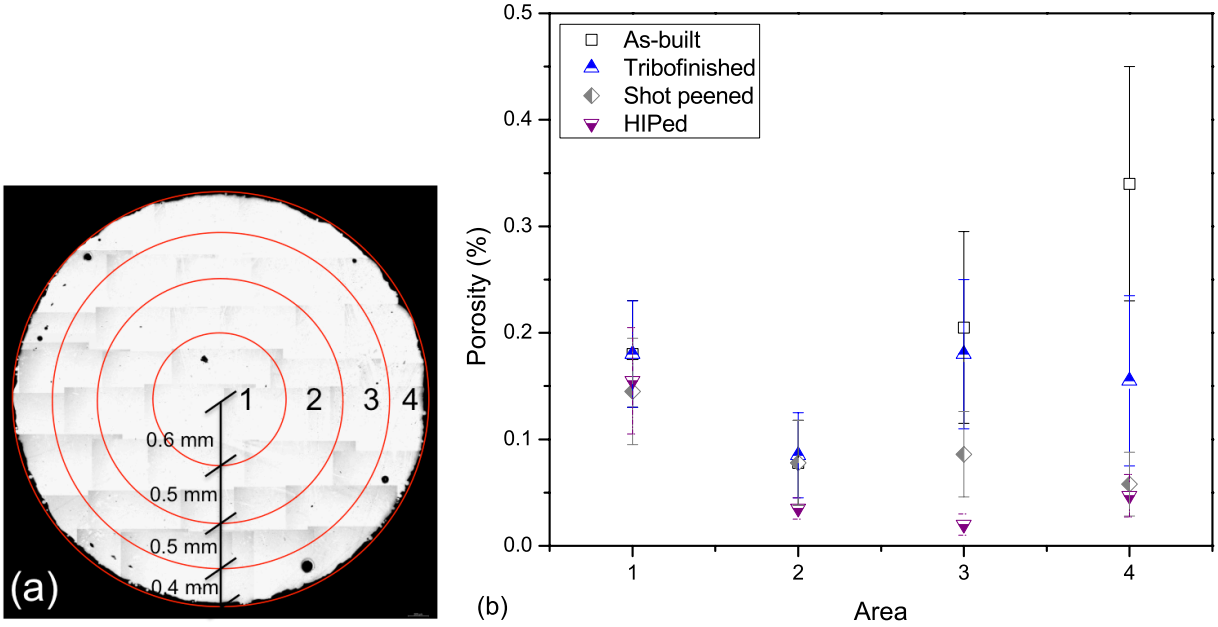
1
2
3
4
0.6 mm
0.5 mm
0.5 mm
0.4 mm
(a)
As-built
Tribofinished
Shot peened
HIPed
Porosity (%)
0.0
0.1
0.2
0.3
0.4
0.5
1
2
3
4
Area
(b)

Fig. 5

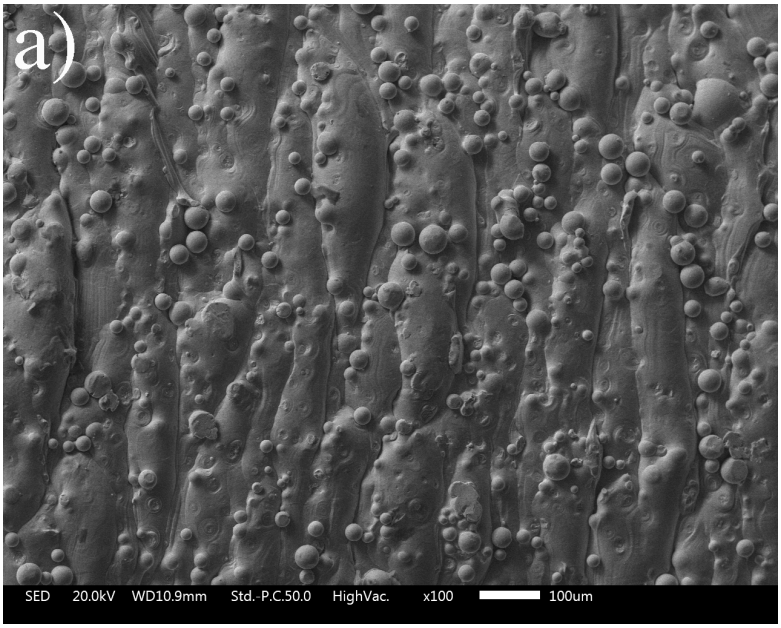
a)
SED 20.0kV WD10.9mm Std.-P.C.50.0 HighVac. x100 100um

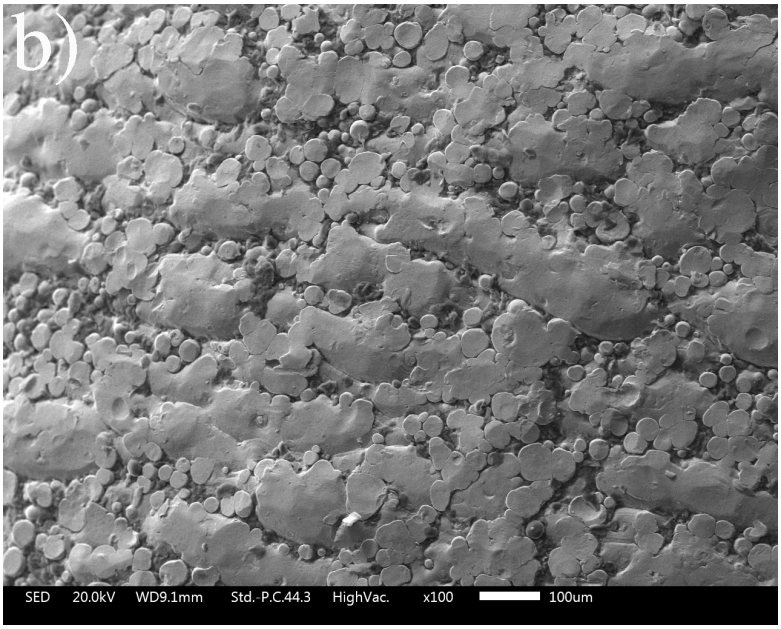
b)
SED 20.0kV WD9.1mm Std.-P.C.44.3 HighVac. x100 100um

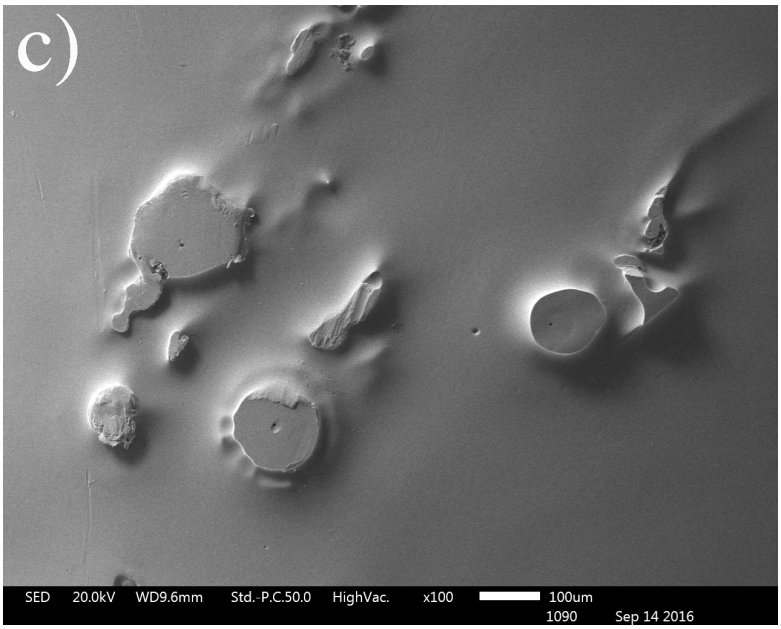
c)
SED 20.0kV WD9.6mm Std.-P.C.50.0 HighVac. x100 100um
1090 Sep 14 2016

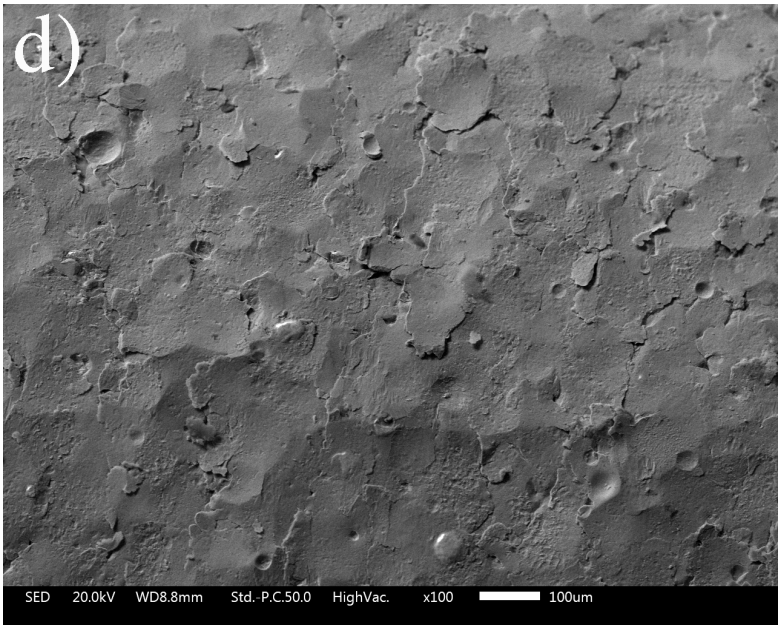
d)
SED 20.0kV WD8.8mm Std.-P.C.50.0 HighVac. x100 100um

Fig. 6

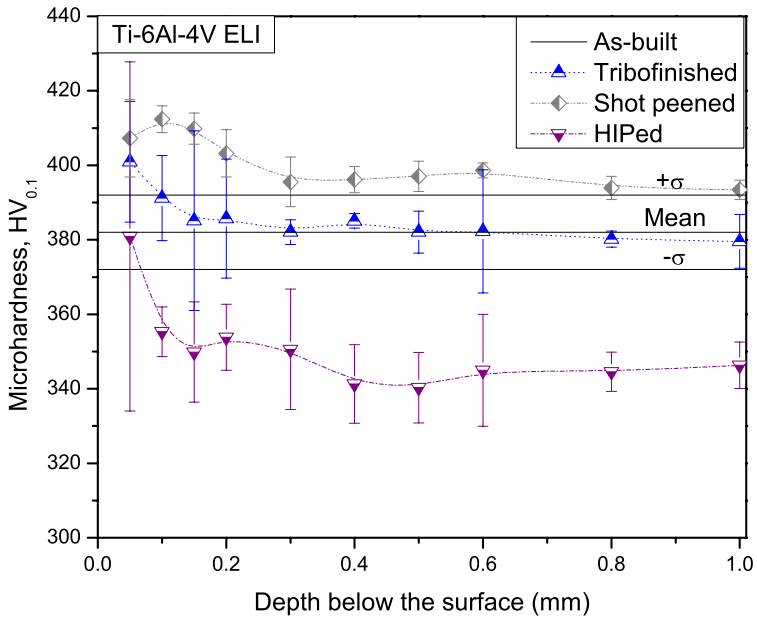
Ti-6Al-4V ELI
As-built
Tribofinished
Shot peened
HIPed
+σ
Mean
-σ
Microhardness, HV0.1
Depth below the surface (mm)
440
420
400
380
360
340
320
300
0.0
0.2
0.4
0.6
0.8
1.0

Fig. 7

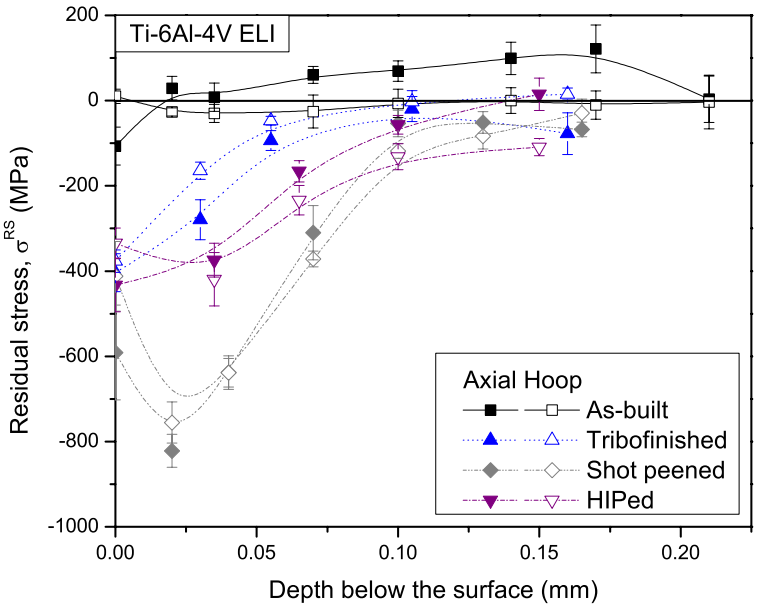
Ti-6Al-4V ELI
Residual stress, σ^{RS} (MPa)
Depth below the surface (mm)
Axial Hoop
As-built
Tribofinished
Shot peened
HIPed

Fig. 8

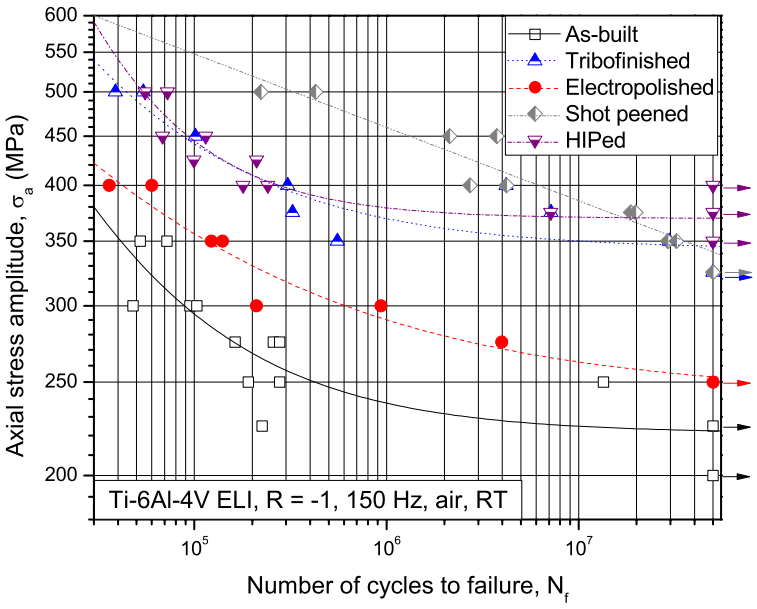
Axial stress amplitude, σ_a (MPa)
Number of cycles to failure, N_f
As-built
Tribofinished
Electropolished
Shot peened
HIPed
Ti-6Al-4V ELI, R = -1, 150 Hz, air, RT

Fig. 9

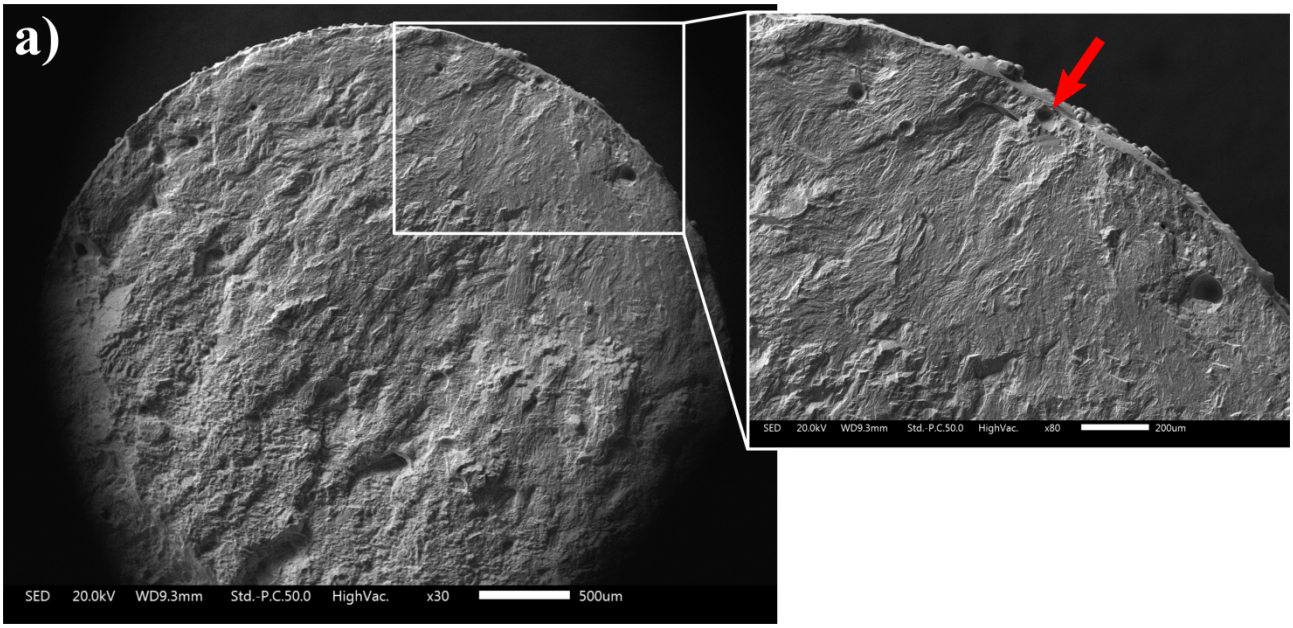
a)
SED 20.0kV WD9.3mm Std.-P.C.50.0 HighVac. x30 500um
SED 20.0kV WD9.3mm Std.-P.C.50.0 HighVac. x80 200um

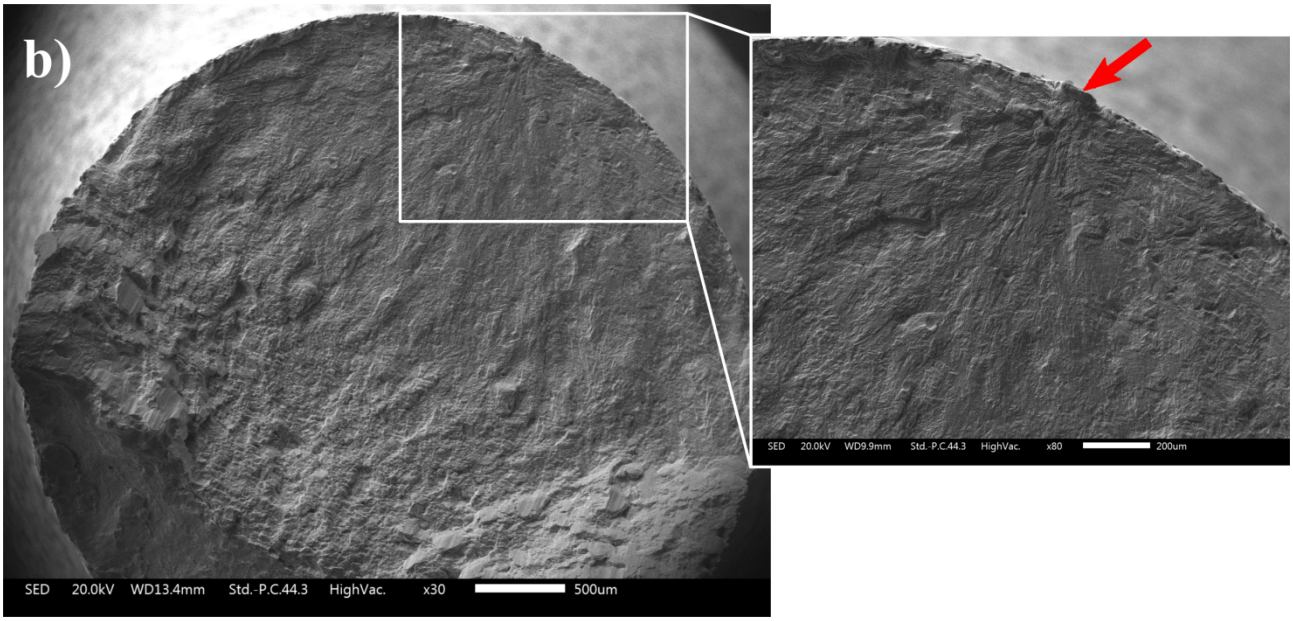
b)
SED 20.0kV WD13.4mm Std.-P.C.44.3 HighVac. x30 500um
SED 20.0kV WD9.9mm Std.-P.C.44.3 HighVac. x80 200um

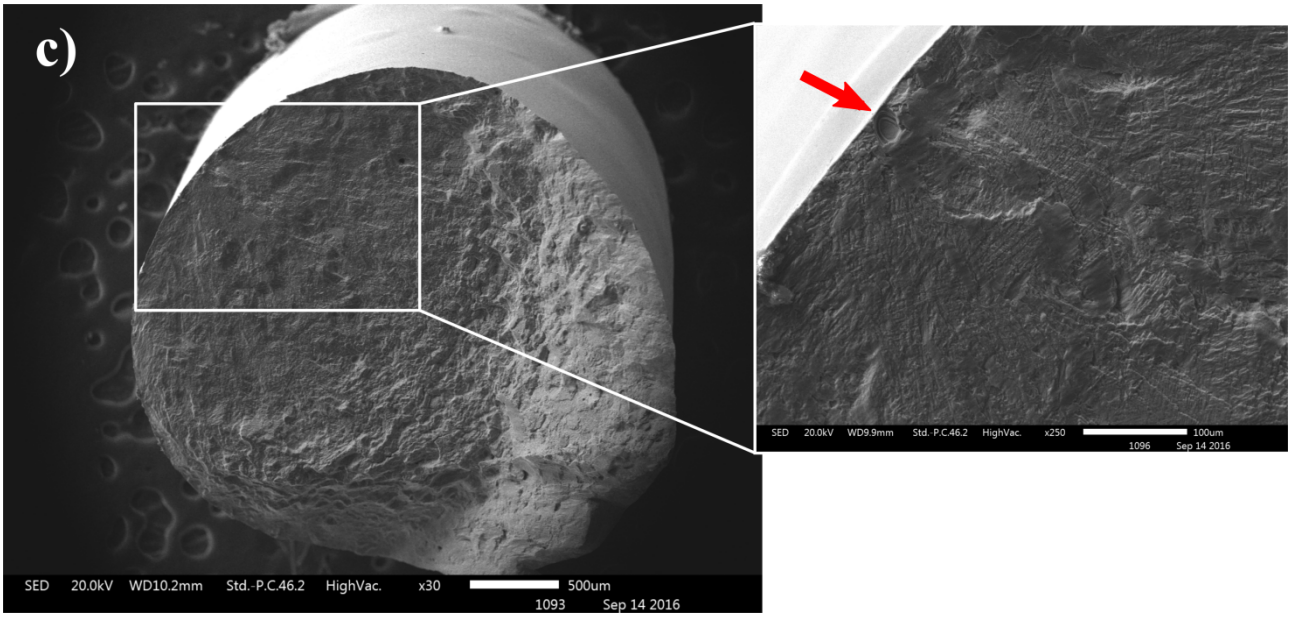
c)
SED 20.0kV WD10.2mm Std.-P.C.46.2 HighVac. x30 500um
1093 Sep 14 2016
SED 20.0kV WD9.9mm Std.-P.C.46.2 HighVac. x250 100um
1096 Sep 14 2016

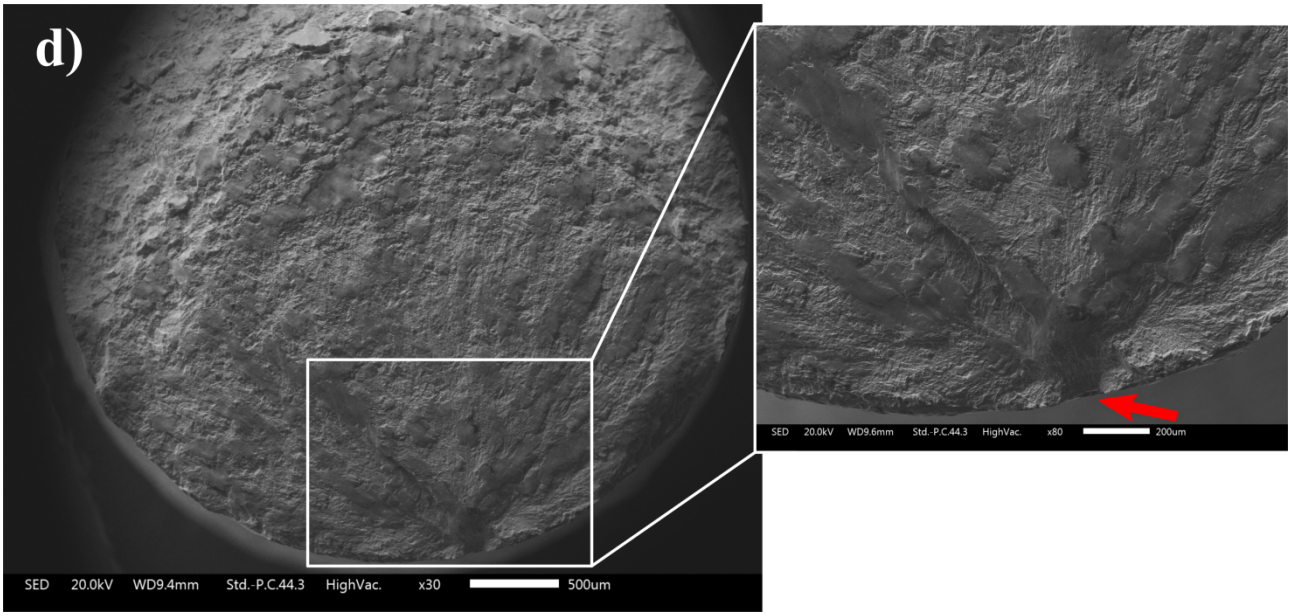
d)
SED 20.0kV WD9.4mm Std.-P.C.44.3 HighVac. x30 500um
SED 20.0kV WD9.6mm Std.-P.C.44.3 HighVac. x80 200um

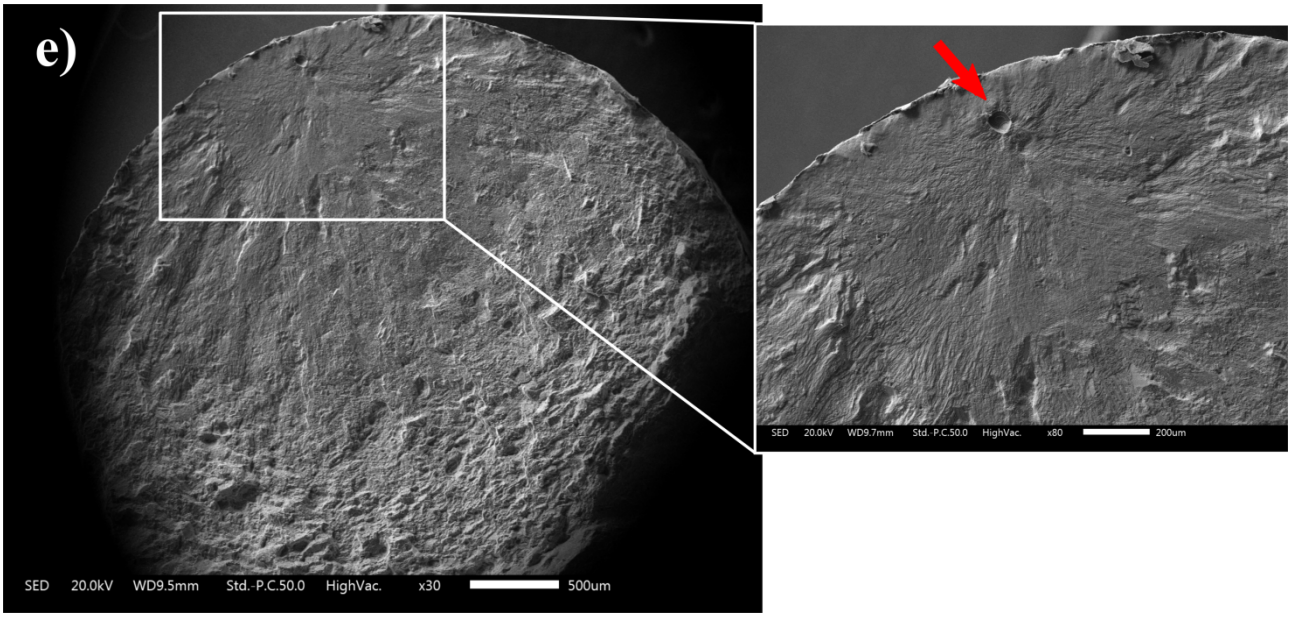
e)
SED 20.0kV WD9.5mm Std.-P.C.50.0 HighVac. x30 500um
SED 20.0kV WD9.7mm Std.-P.C.50.0 HighVac. x80 200um

Fig. 10

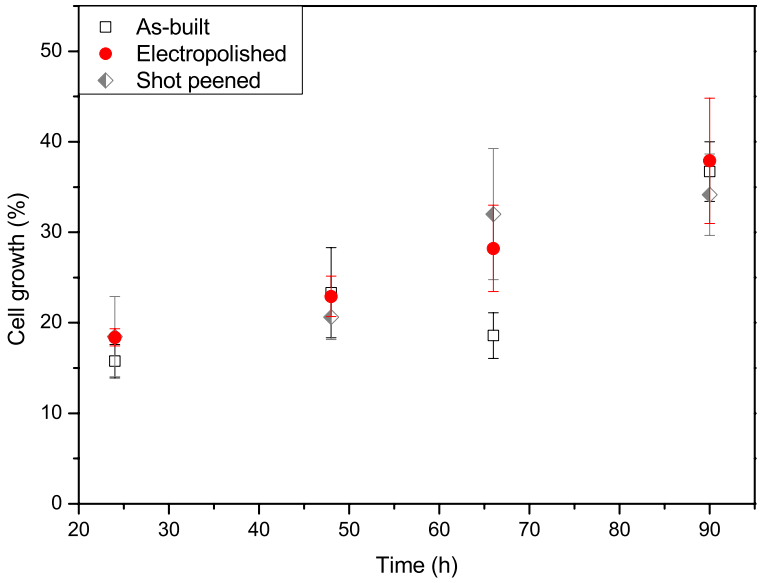
As-built
Electropolished
Shot peened
Cell growth (%)
Time (h)
0
10
20
30
40
50
20
30
40
50
60
70
80
90

Fig. 11.